第 49 卷 第 16 期/2022 年 8 月/中国激光 研究论文

中国激光

基于 BP 神经网络补偿卡尔曼滤波的激光-MIG 复合焊缝熔宽在线检测

刘秀航，黄宇辉，张艳喜，高向东*

广东工业大学广东省焊接工程技术研究中心，中国 广州 510006

摘要 焊缝熔宽是评估焊接质量和焊接稳定性的重要指标。针对强噪声环境下的激光-MIG 复合焊接过程，本文研究了基于反向传播(BP)神经网络补偿色噪声卡尔曼滤波算法的熔宽检测方法。首先建立激光-MIG 复合焊缝熔宽检测系统的状态方程和测量方程，通过视觉传感和色噪声卡尔曼滤波算法对焊缝熔宽进行估计；然后采用高精度激光扫描仪对焊缝的三维轮廓进行扫描，根据二阶差分法获得焊缝轮廓宽度，并将其作为熔宽的真实值；接着将卡尔曼滤波增益、新息值和预测值与卡尔曼滤波最优估计之差作为输入，利用 BP 神经网络对熔宽的卡尔曼滤波最优估计进行补偿。结果表明：BP 神经网络补偿测量色噪声卡尔曼滤波算法能够有效降低焊缝熔宽检测的误差。与单独使用卡尔曼滤波算法相比，BP 神经网络补偿卡尔曼滤波算法具有更好的非线性映射能力，可以提高卡尔曼滤波焊缝熔宽检测的准确度。

关键词 激光技术；神经网络；激光-MIG 复合焊接；熔宽预测；强噪声；卡尔曼滤波

中图分类号 TG409 **文献标志码** A **DOI**：10.3788/CJL202249.1602011

1 引 言

激光-电弧复合焊接是一种结合了激光和电弧两种热源的连接方法，具有激光功率密度高、焊道深宽比大的特点，激光和电弧的复合对电弧和熔滴过渡具有稳定作用[1]。在激光-电弧复合焊接中，电弧的热影响区大，具有良好的桥接性能，能提高焊件对激光的吸收率[2-3]。激光与电弧这两种热源的顺序及其作用范围对焊缝的成形质量至关重要[4-5]，同时焊缝成形也与复合焊接过程中熔滴过渡的形式密切相关[6]。熔宽是衡量焊接质量和焊接稳定性的重要指标。受焊接过程中弧光、反光、飞溅和金属蒸气的干扰，焊接过程中熔宽的视觉检测以及特征提取十分困难。

在激光-电弧复合焊接中，熔宽与金属蒸气特征及熔池的其他特征紧密相关，将熔宽与其他特征相结合可实现焊接状态或焊接质量的有效检测。因此，熔宽检测成为诸多学者的重点研究对象之一[7-8]。目前，光学视觉检测方法因可获得大量可靠的熔池、匙孔和金属蒸气等形态特征数据而被广泛应用于熔宽检测[9]中。Wang 等[10]通过边缘提取算法提取了焊接过程中的熔池轮廓，采用生成对抗网络来扩充数据集，并使用反向传播(BP)神经网络来预测焊缝熔宽。Luo 等[11]利用基于非轴向绿色照明激光器和同轴图像采集系统的焊缝边缘检测技术，实现了强噪声环境下熔池宽度和三维多相模型的预测。陈子琴等[12]建立了贝叶斯神经网络预测模型，并利用焊接过程中的正面视觉传感特征信号对焊缝背部的成形宽度进行了预测。钦兰云等[13]采用卡尔曼滤波技术对熔池图像进行处理，然后将所得的熔池宽度测量数据进行去噪处理，建立了高精度熔宽检测模型。

本文提出了一种针对焊接强噪声环境下实时检测熔宽的方法。激光-MIG 复合焊接将激光焊接技术与熔化极惰性气体保护焊(MIG)结合在一起，可以克服各自的缺点，获得优质焊接接头。为获取激光-MIG 复合焊接过程中的熔池信息，本研究团队采用高速摄像机采集熔池图像，并采用自动标记的分水岭算法分割出图像中的熔池部分。为减小熔池复杂的热分布、流动、受力以及冷却过程对熔宽预测的影响[14-15]，进而减小熔池图像处理计算所得的熔宽与实际焊缝熔宽的误差，本研究团队利用高精度激光三维扫描仪对焊缝轮廓进行扫描，采用二阶差分法从扫描轮廓中提取焊缝熔宽，并采用卡尔曼滤波算法获得熔宽的最优估计值。最后，本研究团队基于 BP 神经网络对卡尔曼滤波最优估计值与真实熔宽的差值进行了预测。

收稿日期：2021-10-19；**修回日期**：2021-11-13；**录用日期**：2021-12-22

基金项目：广州市科技计划(202002020068，202002030147)

通信作者：*gaoxd666@126.com

2 激光-MIG 复合焊接过程检测

2.1 检测装置

激光-MIG 复合焊接试验平台由光纤激光器、六轴机器人、伺服运动平台、保护气体和高速摄像机组成，如图 1 所示。光纤激光器的最大输出功率为 4 kW，六轴机器人和伺服运动平台控制激光焊接头和 MIG 焊枪的位置。高速摄像机采集图像的像素为 640 pixel×480 pixel，采集帧率为 2000 frame/s。用高速摄像机搭配窄带近红外滤光系统提取熔池和匙孔信息。保护气由氩气和 CO_2 组成，二者的体积比为 49∶1。焊件尺寸为 200 mm×100 mm×3 mm，焊丝材料为 ER308 不锈钢。焊接采用电弧辅助激光焊接的方式，激光在前，MIG 焊枪在后。高速相机、激光头和电弧焊枪固定，工件装夹在运动平台上，并在运动平台的带动下运动。高速摄像机从侧面对焊接过程进行拍摄，镜头距离焊缝约 300 mm，与水平方向的夹角为 30°。

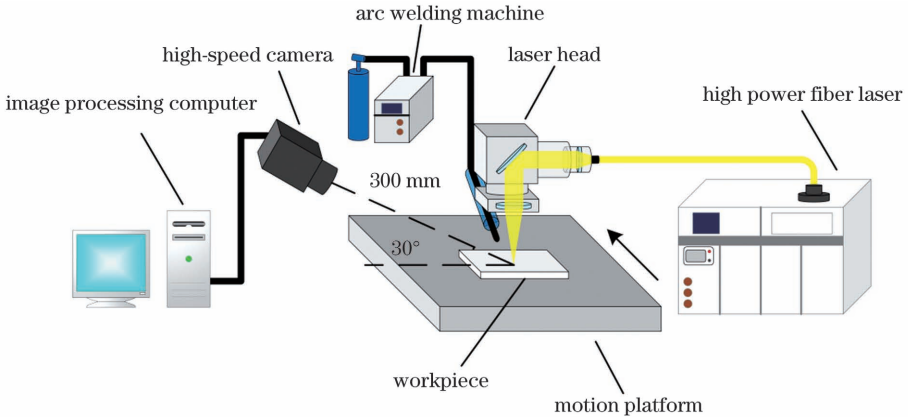

图 1 激光-MIG 复合焊接过程检测系统

Fig. 1 Laser-MIG hybrid welding process detection system

2.2 焊缝成形检测

为了获取熔宽的真实数据，本课题组采用关节臂测量仪搭配激光扫描仪对焊缝正面进行结构光扫描，获取焊缝三维成形轮廓数据。为了从焊缝轮廓中提取出焊缝熔宽，采用二阶差分算法处理轮廓数据，所得二阶差分曲线上两个极大值点之间的间距为焊缝轮廓的真实宽度，如图 2 所示。

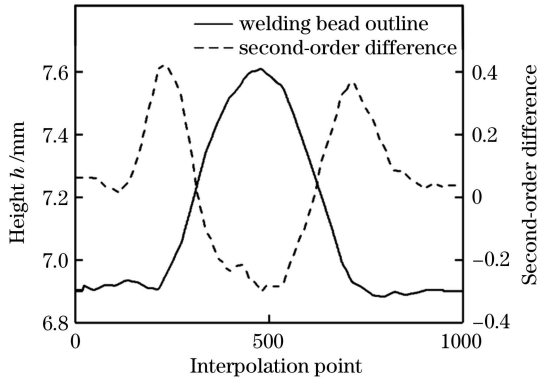

图 2 二阶差分法提取焊缝成形宽度

Fig. 2 Weld forming width extraction with second-order difference method

3 熔宽特征提取

采用高速摄像机获取焊接过程中的焊接图像。高速摄像机在侧面采集的熔池和匙孔图像如图 3 所示。图 3 中不仅包含了熔宽特征提取所需的熔池区域和匙孔区域的相关信息，还包含了会对特征提取产生遮挡或干扰的弧光、熔滴、熔融部分和焊件表面的反光。

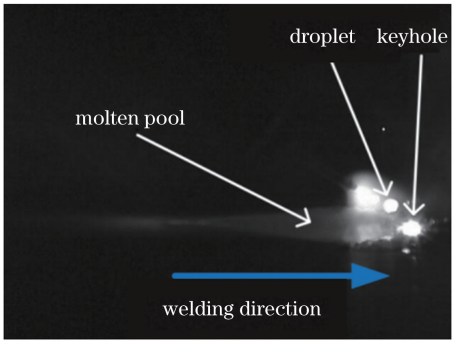

图 3 高速摄像机采集的激光-MIG 复合焊接过程图像

Fig. 3 Laser-MIG hybrid welding process image captured by high-speed camera

分水岭算法是一种基于图像像素灰度值的图像分割方法，以相邻像素的灰度相似程度作为图像分割的判断依据[16-18]。图 4 为高速摄像机采集图的灰度三维

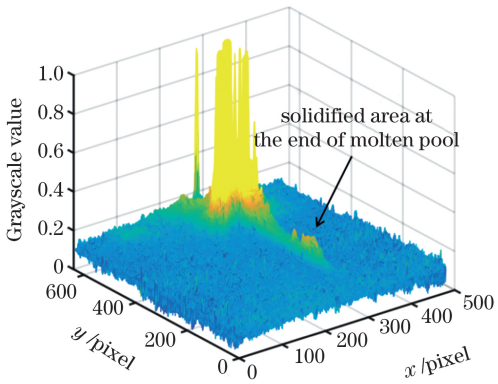

图 4 焊接过程的三维灰度图

Fig. 4 Three-dimensional grayscale image of welding process

图。分析后可以发现，熔池表面处于凝固临界点的部分对弧光的反射相对于其周围液态熔池更为强烈，具有更高的灰度值。因此，可以基于灰度值的差异对熔池尾部的位置进行定位。

图像处理和特征提取方法如下：首先提取图像的感兴趣区域，并采用高斯滤波对图像进行预处理，得到图 5(a)；然后取匙孔到熔池尾部之间的连线作为熔池位置的标记，如图 5(b)所示，采用分水岭算法对标记部分的图像进行分割，分割出的熔池如图 5(c)所示；最后对图像进行形态学处理，得到图 5(d)。

为了提取分割后的熔池宽度，取每帧图像上熔池纵向宽度的最大值作为测量的熔池宽度。对不锈钢激光-MIG 复合焊接过程中熔池的像素宽度与实际宽度进行标定，实现图像像素与真实尺寸的转换。高速摄像机在录像模式下采集的图像的纵向最大尺寸为 480 pixel，图中纵向宽度为 67 mm。通过对比图 5(a)和图 5(d)可知，采用形态学处理获得的熔池宽度与原始图像中的熔池宽度相差约 1 pixel，证明形态学处理得到的熔池宽度精确可靠。通过计算得到真实熔池宽度的 1 mm 对应图中约 7.16 pixel，即

$$x_t = x_p / 7.16, \tag{1}$$

式中：x_t 为熔池的真实宽度，单位为 mm；x_p 为熔池的像素宽度，单位为 pixel。图 6 为熔宽测量值和真实值的对比图。不难看出，在标注的虚线(黄线)范围内测量的焊缝熔宽峰值与真实的焊缝熔宽峰值相对应，且两者整体变化趋势相近。但是，受强噪声干扰以及熔池复杂流动特性的影响，测量值与真实值之间仍存在较大误差。

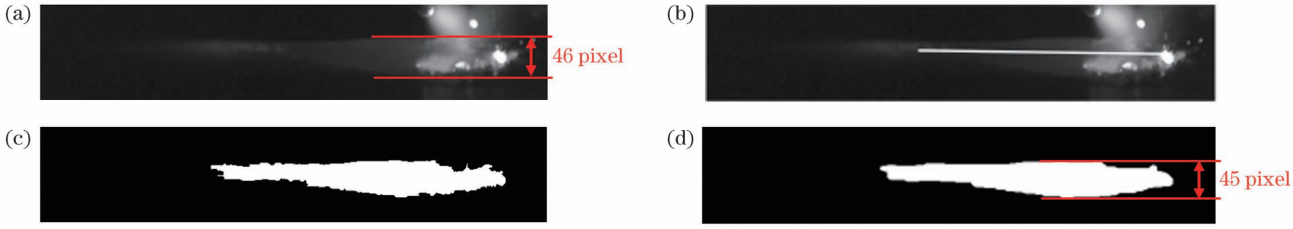

图 5 激光-MIG 复合焊接熔池图像的处理过程。(a)提取感兴趣区域；(b)标记熔池；(c)分水岭算法分割图像；(d)形态学处理

Fig. 5 Processing of laser -MIG hybrid welding molten pool image. (a) Extraction of region of interest (ROI); (b) mark of a molten pool; (c) image segmentation with watershed algorithm; (d) morphological processing

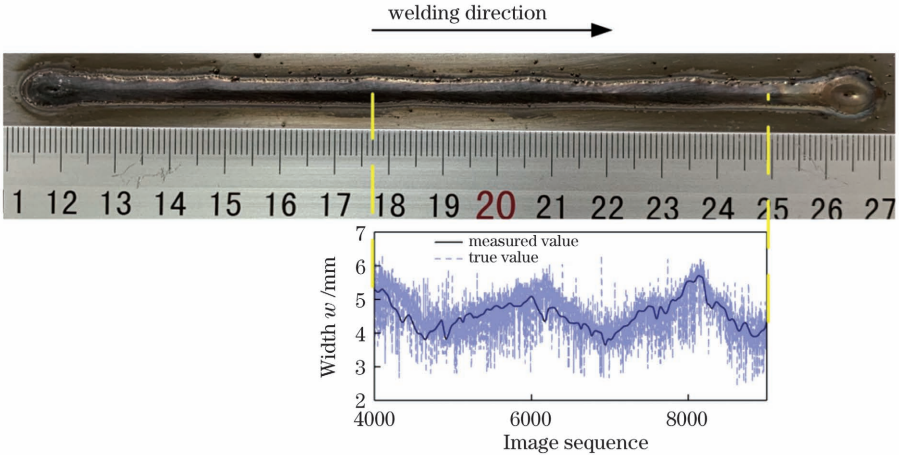

图 6 熔宽测量值与真实值的对比

Fig. 6 Comparison of measured and true weld widths

4 BP 神经网络补偿测量色噪声卡尔曼滤波预测焊缝熔宽

熔池不仅蕴含着丰富的焊接信息，其特征也关乎着焊缝成形的形态，因此可以根据熔池宽度来检测焊缝的宽度。卡尔曼滤波算法在焊接检测和跟踪上的应用十分广泛[19-22]。为建立熔池宽度与焊缝熔宽之间的联系，本研究团队利用卡尔曼滤波技术建立被测对象的状态方程和测量方程，采用递推算法不断调整卡尔曼增益，通过估算概率分布和测量误差导致的概率分布，在二者之中求出最优估计值。由于在激光-MIG 复合焊接熔池宽度的检测中，弧光、飞溅产生的有色噪声会对检测结果产生一定影响，因此需要采用测量色噪声卡尔曼滤波算法对熔宽进行检测，并利用 BP 神经网络对卡尔曼滤波最优估计值进行补偿。

4.1 测量色噪声状态方程和测量方程的建立

本文假设系统的状态噪声的方差为 1×10^{-5}，则系统的过程噪声为

$$\boldsymbol{Q} = \begin{bmatrix} 1\times10^{-5} & 0 & 0 \\ 0 & 1\times10^{-5} & 0 \\ 0 & 0 & 1\times10^{-5} \end{bmatrix}。 \tag{2}$$

假设测量噪声的协方差矩阵为

$$\boldsymbol{R}=\begin{bmatrix}0.5 & 0\\ 0 & 0.5\end{bmatrix}。\tag{3}$$

定义 x_1、x_2、x_3 分别为当前时刻的熔宽、熔池宽度变化的速度和上一时刻的熔宽，则熔池宽度检测系统的状态方程为

$$\begin{bmatrix}x_1(k+1)\\ x_2(k+1)\\ x_3(k+1)\end{bmatrix}=\begin{bmatrix}1 & t & 0\\ 0 & 1 & 0\\ 1 & 0 & 0\end{bmatrix}\begin{bmatrix}x_1(k)\\ x_2(k)\\ x_3(k)\end{bmatrix}+\begin{bmatrix}0.5t^2\\ t\\ 0\end{bmatrix}\omega(k),\tag{4}$$

式(4)可简化为

$$\boldsymbol{X}(k+1)=\boldsymbol{A}(t)\boldsymbol{X}(k)+\boldsymbol{B}(t)\omega(k),\tag{5}$$

式中：$\boldsymbol{X}(k+1)$为 $k+1$ 时刻系统的状态向量；$\boldsymbol{X}(k)$为 k 时刻系统的状态向量；$\boldsymbol{A}(t)$为系统的状态转移矩阵；$\omega(k)$为 k 时刻的过程噪声；$\omega(k)$为随机加速度；t 为采样时间。

测量色噪声卡尔曼滤波的测量方程为

$$\begin{bmatrix}x(k)\\ \Delta x(k)\end{bmatrix}=\begin{bmatrix}0.5 & 1 & 0\\ -0.5 & 1 & 0.5\end{bmatrix}\begin{bmatrix}x_1(k)\\ x_2(k)\\ x_3(k)\end{bmatrix}+\boldsymbol{V}(k),\tag{6}$$

式(6)可简化为

$$\boldsymbol{Z}(k)=\boldsymbol{H}\boldsymbol{X}(k)+\boldsymbol{V}(k),\tag{7}$$

式中：Δx 为位移量；$\boldsymbol{Z}(k)$为 k 时刻的测量向量；$\boldsymbol{H}$ 为 k 时刻的测量矩阵；$\boldsymbol{V}(k)$为 k 时刻系统的测量噪声。使用测量扩增的方法来白化测量色噪声，其中测量色噪声满足一阶自回归模型，即

$$\begin{bmatrix}v_x(k)\\ v_{\Delta x}(k)\end{bmatrix}=\begin{bmatrix}0.5 & 0\\ 0 & 0.5\end{bmatrix}\begin{bmatrix}v_x(k-1)\\ v_{\Delta x}(k-1)\end{bmatrix}+\begin{bmatrix}\eta_x(k-1)\\ \eta_{\Delta x}(k-1)\end{bmatrix},\tag{8}$$

式中：$v_x(k)$和 $v_x(k-1)$分别为 k 时刻和 $k-1$ 时刻的熔宽测量值；$v_{\Delta x}(k)$和 $v_{\Delta x}(k-1)$分别为 k 时刻、$k-1$ 时刻与前一时刻熔宽的差值；$\eta_x(k-1)$和 $\eta_{\Delta x}(k-1)$分别为均值为 0、方差为 $\boldsymbol{R}$ 的噪声序列。式(8)可简化为

$$\boldsymbol{V}(k+1)=\boldsymbol{\Psi}(k\,|\,k-1)\boldsymbol{V}(k-1)+\boldsymbol{\eta}(k-1),\tag{9}$$

式中：$\boldsymbol{\eta}(k-1)$表示方差为 $\boldsymbol{R}$ 的高斯白噪声。

修正后的测量色噪声卡尔曼递推算法公式为

$$\boldsymbol{S}(k)=\boldsymbol{Q}(k)\boldsymbol{B}^{\mathrm{T}}(k)\boldsymbol{H}(k),\tag{10}$$

$$\boldsymbol{J}(k)=\boldsymbol{B}(k)\boldsymbol{S}(k)\boldsymbol{R}^{\mathrm{T}}(k),\tag{11}$$

$$\boldsymbol{X}(k+1\mid k)=\boldsymbol{A}\boldsymbol{X}(k\mid k)+\boldsymbol{J}(k)[\boldsymbol{Z}(k)-\boldsymbol{H}(k)\boldsymbol{X}(k\mid k)],\tag{12}$$

$$\begin{aligned}\boldsymbol{P}(k\mid k-1)=&[\boldsymbol{A}-\boldsymbol{J}(k-1)\boldsymbol{H}(k-1)]\boldsymbol{P}(k-1)[\boldsymbol{A}-\boldsymbol{J}(k-1)\boldsymbol{H}(k-1)]^{\mathrm{T}}+\\ &\boldsymbol{B}(k-1)\boldsymbol{Q}(k-1)\boldsymbol{B}^{\mathrm{T}}(k-1)-\boldsymbol{J}(k-1)\boldsymbol{S}^{\mathrm{T}}(k-1)\boldsymbol{B}^{\mathrm{T}}(k-1),\end{aligned}\tag{13}$$

$$\widetilde{\boldsymbol{Y}}(k+1)=\boldsymbol{Y}(k+1)-\boldsymbol{H}\boldsymbol{X}(k+1\,|\,k),\tag{14}$$

$$\boldsymbol{K}(k)=\boldsymbol{P}(k\mid k-1)\boldsymbol{H}^{\mathrm{T}}(k)[\boldsymbol{H}(k)\boldsymbol{P}(k\mid k-1)\boldsymbol{H}^{\mathrm{T}}+\boldsymbol{R}(k)]^{-1},\tag{15}$$

$$\boldsymbol{X}(k\,|\,k)=\boldsymbol{A}\boldsymbol{X}(k\,|\,k-1)+\boldsymbol{K}(k)\widetilde{\boldsymbol{Y}}(k),\tag{16}$$

$$\boldsymbol{P}(k\,|\,k)=[\boldsymbol{I}_{\mathrm{n}}-\boldsymbol{K}(k)\boldsymbol{H}(k)]\boldsymbol{P}(k\,|\,k-1),\tag{17}$$

式中：$\boldsymbol{I}_{\mathrm{n}}$ 为单位矩阵。将所有熔池测量数据按上面的公式依次进行递推处理，就可以获得熔池宽度卡尔曼滤波的最优估计值。

4.2 BP 神经网络补偿卡尔曼滤波

在卡尔曼滤波过程中，建模本身存在的误差会导致卡尔曼滤波精度下降，并使滤波存在发散风险。为此，采用 BP 神经网络对卡尔曼滤波最优估计值与真实值之差这一非线性值进行预测。用神经网络训练的结果来补偿卡尔曼滤波最优估计的误差，可以实现熔宽检测精度的提高。

在实验中，建立具有 5 个隐藏神经元的 BP 神经网络对卡尔曼滤波最优估计值进行补偿，其输入分别为卡尔曼滤波增益 $\boldsymbol{K}(k)$、新息值 $\widetilde{\boldsymbol{Y}}(k+1)$、预测值与卡尔曼滤波最优估计之差 $\boldsymbol{X}(k+1\,|\,k)-\boldsymbol{X}(k\,|\,k)$，输出为卡尔曼滤波最优估计与系统输入之差 $\boldsymbol{X}(k\,|\,k)-\boldsymbol{X}(k)$。

5 焊缝熔宽预测结果与分析

采用激光-MIG 复合焊接实验对 BP 神经网络补偿卡尔曼滤波的焊接熔宽检测结果进行验证。采用平板堆焊的形式进行焊接实验，焊接速度为 1.75 m/min，激光功率为 2.2 kW，电流为 80 A，电压为 18 V，焊接总长度为 150 mm，采用高速摄像机对焊接过程进行图像采集。选取焊接过程中电弧行为较为平稳的连续图像作为熔池面积检测与提取的对象，并将获得的 1300 个实验数据作为熔宽检测对象。对实验数据进行图像处理，提取出熔宽测量值，测量值经过卡尔曼滤波后，得到卡尔曼滤波最优估计值以及对应的卡尔曼滤波过程参数。

为进一步减小焊缝熔宽的检测误差，采用 BP 神经网络对卡尔曼滤波最优估计值进行补偿。将上述数据分为训练集和测试集，随机选取 500 帧连续数据作为测试集，其余数据作为训练集。将训练集样本的卡尔曼滤波过程参数作为 BP 神经网络的输入，并进行训练。完成熔宽检测神经网络的训练后，将剩余的 500 个测试集样本输入至训练好的神经网络中，并用输出的最优估计值与真实值的差值对最优估计值进行补偿。最终检测结果的对比如图 7 所示，可以看出，

BP 神经网络补偿卡尔曼滤波值(BP-KF 值)明显比卡尔曼滤波值(KF 值)对熔宽真实值的拟合情况更好。这表明,BP 神经网络补偿卡尔曼滤波算法检测的熔宽在总体上更接近真实值。

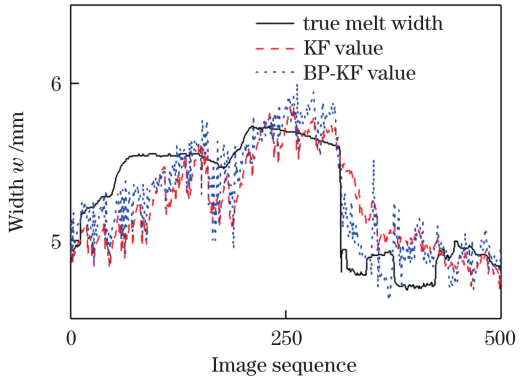

图 7 BP 神经网络补偿卡尔曼滤波值与卡尔曼滤波值的对比

Fig. 7 Comparison of BP neural network compensation Kalman filter (BP-KF) and Kalman filter (KF) values

分别计算 BP-KF 值、KF 值与真实值之间的绝对误差,进一步探索 BP 神经网络对卡尔曼滤波最优估计值与真实值误差的抑制效果,结果如图 8 所示。从图 8 中可以看出 BP-KF 最优估计值与真实值之间的绝对误差总体上要小于 KF 最优估计值与真实值之间的绝对误差,这表明经过 BP 神经网络补偿的熔宽检测值的误差相比未经补偿的熔宽检测值的误差更小,检测效果更好。

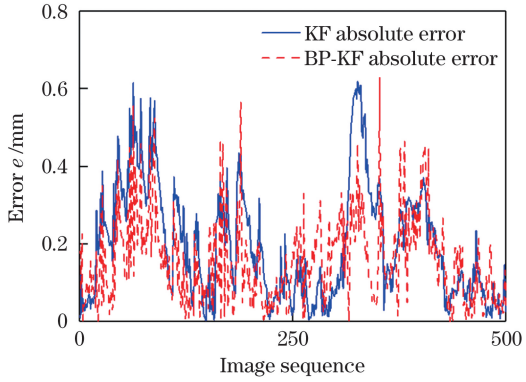

图 8 KF 和 BF-KF 的最优估计值与熔宽真实值之间的绝对误差

Fig. 8 Absolute error values between true weld widths and the estimated value of BP-KF and KF

分别计算图像处理获得的测量值、KF 值和 BP-KF 值与真实值的各项误差,准确对比各种方法对熔宽检测的效果。表 1 为各方法对焊缝熔宽检测的误差统计分析。采用 BP 神经网络补偿卡尔曼滤波算法对焊缝熔宽进行检测时,其最大误差(MAX)、平均绝对误差(MAE)、均方根误差(RMSE)和平均绝对百分比误差(MAPE)相较其他两种算法均进一步降低,同时其均方根误差为 0.16 mm,能满足对焊缝熔宽检测的要求。试验数据表明,BP-KF 算法对激光-MIG 复合焊接焊缝熔宽数据的检测误差具有良好的抑制能力。BP 神经网络补偿值对卡尔曼滤波最优估计值与真实熔宽值之间的误差起到了一定的拟合作用。

表 1 误差统计分析

Table 1 Error statistical analysis

Error	MAX / mm	MAE / mm	RMSE / mm	MAPE / %
Measurement error	2.13	0.33	0.47	7.1
KF error	0.67	0.15	0.20	3.2
BP-KF error	0.65	0.13	0.16	2.7

6 结 论

本课题组首先建立激光-MIG 复合焊接过程检测系统,然后针对激光-MIG 复合焊接过程中强弧光、强反光的影响,采用自动标记的分水岭算法分割熔池区域,有效提取出焊接过程中的熔宽。提取的熔宽与真实的焊缝熔宽之间存在误差,采用测量色噪声卡尔曼滤波算法降低噪声的影响,并通过 BP 神经网络补偿卡尔曼滤波最优估计值与实际值之间的误差来减小图像提取熔宽与真实焊缝熔宽之间的误差。结果显示,BP 神经网络补偿卡尔曼滤波算法的平均绝对百分比误差比图像提取的熔宽误差和卡尔曼滤波算法获取的熔宽误差分别降低了 4.4 个百分点和 0.5 个百分点。相比其他研究中单独采用卡尔曼滤波算法对熔宽测量值进行降噪处理,BP 神经网络预测出的卡尔曼滤波最优估计值与实际值的误差能在卡尔曼滤波算法减小熔宽测量值误差的基础上,进一步提高熔宽的检测精度。该检测方法可以获得比较准确的熔宽,从而可以有效提高激光-MIG 复合焊接过程中焊接状态和焊接质量的检测精度。

参 考 文 献

[1] Ma C Y, Chen B, Tan C W, et al. Characteristics of droplet transfer, molten pool formation, and weld bead formation of oscillating laser hot-wire tungsten inert gas hybrid welding[J]. Journal of Laser Applications, 2021, 33(1): 012027.

[2] 雷正龙, 黎炳蔚, 周恒, 等. 端接接头激光-MAG 复合焊熔滴过渡与气孔特征分析[J]. 中国激光, 2019, 46(3): 0302007.
Lei Z L, Li B W, Zhou H, et al. Analysis of droplet transfer and porosity characteristics in laser-MAG hybrid welding of edge joint[J]. Chinese Journal of Lasers, 2019, 46(3): 0302007.

[3] 刘西洋, 孙凤莲, 赵御民, 等. 自保护药芯焊丝激光-电弧复合热源焊接电弧稳定性的分析[J]. 焊接学报, 2018, 39(7): 17-23, 129.
Liu X Y, Sun F L, Zhao Y M, et al. Analysis of arc stability of self-shielded flux-cored wire laser-arc hybrid[J]. Transactions of the China Welding Institution, 2018, 39(7): 17-23, 129.

[4] 刘政君, 顾思远, 张培磊, 等. 高强钢激光-MIG 复合焊对接间隙下的焊缝成形机理[J]. 中国激光, 2019, 46(9): 0902006.
Liu Z J, Gu S Y, Zhang P L, et al. Welding seam forming mechanism of high-strength steel laser-metal inert gas hybrid welding with butt gap[J]. Chinese Journal of Lasers, 2019, 46(9): 0902006.

[5] 李昊岳, 檀财旺, 张强, 等. 热源顺序对 HG785D 高强钢激光-电弧复合焊耦合机理与接头性能的影响[J]. 中国激光, 2018,

45(5): 0502006.
Li H Y, Tan C W, Zhang Q, et al. Effect of heat source order on coupling mechanism and mechanical properties of joints in laser-arc hybrid welding of HG785D high-strength steels[J]. Chinese Journal of Lasers, 2018, 45(5): 0502006.
[6] 任闻杰, 郑惠锦, 李铸国, 等. 脉冲电弧对激光脉冲电弧复合焊熔滴过渡与飞溅的影响[J]. 中国激光, 2020, 47(4): 0402007.
Ren W J, Zheng H J, Li Z G, et al. Effects of pulse arc on droplet transfer and spatter of laser pulsed-arc hybrid welding [J]. Chinese Journal of Lasers, 2020, 47(4): 0402007.
[7] 王煜, 高向东, 陈子琴, 等. 激光-MAG 复合焊接过程金属蒸气和背部熔池图像分析[J]. 机械工程学报, 2019, 55(19): 167-173.
Wang Y, Gao X D, Chen Z Q, et al. Analysis of the images of metal vapor and bottom-molten pool in laser-MAG hybrid welding process[J]. Journal of Mechanical Engineering, 2019, 55(19): 167-173.
[8] Peng G D, Chang B H, Xue B C, et al. Closed-loop control of medium-thickness plate arc welding based on weld-face vision sensing [J]. Journal of Manufacturing Processes, 2021, 68: 371-382.
[9] Cai W, Wang J Z, Jiang P, et al. Application of sensing techniques and artificial intelligence-based methods to laser welding real-time monitoring: a critical review of recent literature [J]. Journal of Manufacturing Systems, 2020, 57: 1-18.
[10] Wang Y M, Han J, Lu J, et al. TIG stainless steel molten pool contour detection and weld width prediction based on Res-Seg [J]. Metals, 2020, 10(11): 1495.
[11] Luo M, Shin Y C. Vision-based weld pool boundary extraction and width measurement during keyhole fiber laser welding[J]. Optics and Lasers in Engineering, 2015, 64: 59-70.
[12] 陈子琴, 高向东, 王煜, 等. 大功率激光焊背面焊缝宽度神经网络预测[J]. 焊接学报, 2018, 39(11): 48-52, 131.
Chen Z Q, Gao X D, Wang Y, et al. Weldment back of weld width prediction based on neural network during high-power laser welding[J]. Transactions of the China Welding Institution, 2018, 39(11): 48-52, 131.
[13] 钦兰云, 徐丽丽, 杨光, 等. 激光沉积成形熔池尺寸分析与预测[J]. 红外与激光工程, 2018, 47(11): 1106009.
Qin L Y, Xu L L, Yang G, et al. Analysis and prediction of melt pool size in laser deposition manufacturing[J]. Infrared and Laser Engineering, 2018, 47(11): 1106009.
[14] Yan T Y, Zhan X H, Gao Q Y, et al. Influence of laser power on molten pool flow field of laser-MIG hybrid welded Invar alloy [J]. Optics & Laser Technology, 2021, 133: 106539.
[15] Chen X Y, Yu G, He X L, et al. Numerical study of heat transfer and solute distribution in hybrid laser-MIG welding[J]. International Journal of Thermal Sciences, 2020, 149(3): 106182.
[16] 黄亮, 姚丙秀, 陈朋弟, 等. 融合层次聚类的高分辨率遥感影像超像素分割方法[J]. 红外与毫米波学报, 2020, 39(2): 263-272.
Huang L, Yao B X, Chen P D, et al. Superpixel segmentation method of high resolution remote sensing images based on hierarchical clustering[J]. Journal of Infrared and Millimeter Waves, 2020, 39(2): 263-272.
[17] Haag S, Shakibajahromi B, Shokoufandeh A. A new rapid watershed delineation algorithm for 2D flow direction grids[J]. Environmental Modelling & Software, 2018, 109: 420-428.
[18] Haag S, Schwartz D, Shakibajahromi B, et al. A fast algorithm to delineate watershed boundaries for simple geometries [J]. Environmental Modelling & Software, 2020, 134: 104842.
[19] 张益溢, 吴佳琛, 郝然, 等. 基于数字全息的血红细胞显微成像技术[J]. 物理学报, 2020, 69(16): 20200357.
Zhang Y Y, Wu J C, Hao R, et al. Digital holographic microscopy for red blood cell imaging[J]. Acta Physica Sinica, 2020, 69(16): 20200357.
[20] 董航, 丛明, Zhang Yuming, 等. 基于 KF-GPR 的熔池关键特征建模方法[J]. 焊接学报, 2018, 39(12): 49-52, 131.
Dong H, Cong M, Zhang Y M, et al. Characteristic performance modeling method for weld pool based on KF-GPR [J]. Transactions of the China Welding Institution, 2018, 39(12): 49-52, 131.
[21] Gao X D, Zhong X G, You D Y, et al. Kalman filtering compensated by radial basis function neural network for seam tracking of laser welding [J]. IEEE Transactions on Control Systems Technology, 2013, 21(5): 1916-1923.
[22] Gao X D, Chen Y Q, You D Y, et al. Detection of micro gap weld joint by using magneto-optical imaging and Kalman filtering compensated with RBF neural network[J]. Mechanical Systems and Signal Processing, 2017, 84: 570-583.

Online Weld Width Detection of Laser-MIG Hybrid Welding Based on Kalman Filter Algorithm Compensated by BP Neural Network

Liu Xiuhang, Huang Yuhui, Zhang Yanxi, Gao Xiangdong*

Guangdong Provincial Welding Engineering Technology Research Center, Guangdong University of Technology, Guangzhou 510006, Guangdong, China

Abstract

Objective For decades, laser-arc hybrid welding has gained remarkable attention as a reliable technology for material joint processing. It has been applied to various fields of the manufacturing industry due to several characteristics, such as deep penetration, high welding speed, and high-quality shaping. In the laser-arc hybrid welding process, the change in parameters may deeply influence the weld formation. To detect weld defects or monitor the quality of welding beads, several scholars have studied and explored the correlation between welding features and quality. Thus, numerous studies have investigated the relationship between metallic vapor features and molten pools. Among these features, weld width is a crucial evaluation criterion for welding quality and stability. It is commonly acknowledged that high-speed cameras are widely used to capture all types of features during laser-arc hybrid welding. This study presents an online detection of weld width based on the Kalman filter algorithm (BP-KF), which is compensated by a back-propagation neural network and can detect accurate weld width in a strong noise laser-MIG hybrid-welding environment. We assume that our innovative approach can provide the basis for online detection of a laser-arc hybrid-welding process.

Methods The laser-MIG hybrid-welding detection system was established using a high-speed camera, arc welding machine, power fiber laser, and an image processing personal computer. During laser-arc hybrid welding, a high-speed camera was used to collect an image of a molten pool outline. Note that image processing is crucial for obtaining the width of the molten pool from an image. First, a molten pool area was defined and extracted by processing the sequential images emerging from the camera. Next, the end of the molten pool was identified by the difference of gray value in the image, and the keyhole was used to mark the position of the molten pool. After segmenting the image using a watershed algorithm, the width of the molten pool can be measured using the conversion from the pixel to the unit of distance. A high-precision laser scanner was used to scan the three-dimensional contour of the weld, and the width of the weld contour was obtained using the second-order difference method, which was used as the approximate true value of the weld width. According to the state and measurement equations of the laser-MIG hybrid welding width detection system, the weld width was estimated using visual sensing and colored measurement noise Kalman filter (KF) algorithm. Finally, the Kalman filter gain, new information, and difference between the predicted value and the Kalman optimal estimation were taken as the inputs. After obtaining the difference between Kalman optimal estimation and true weld width, the Kalman optimal estimation of the weld width was compensated by the BP neural network to improve the accuracy of weld-width detection.

Results and Discussions Based on the comparison of the measured weld width and true values, both values with observable differences had the same variation tendency (Fig. 6). To decrease the errors between the measured and true weld width values, the colored measurement noise Kalman filter algorithm was adopted to restrain errors from noise. However, the Kalman filter algorithm could not further eliminate these errors. Therefore, to enhance accuracy, the BP neural network was used to predict nonlinear errors caused by the fluctuation of the molten pool. After comparing the weld width values with true weld width, KF, and BP-KF, we observed that the values from BP-KF were generally closer to the true values than those from KF (Fig. 7). The absolute errors between the true values and values from KF or BP-KF were calculated, BP-KF absolute errors were less than that of KF, which indicates that BP-KF can further decrease the errors between measurements and true values (Fig. 8). Based on the abovementioned difference, the errors from the molten pool measurement, KF, and BP-KF were analyzed. It was crucial to demonstrate that weld width errors from BP-KF were less than others, such as max, mean-absolute, root-mean-square, and mean-absolute percentage errors (Table 1). Particularly, the weld width detected by BP-KF can satisfy the demands of manufacturers.

Conclusions This study successfully adopts the watershed image segmentation approach to extract weld width in a strong noise laser-MIG hybrid-welding environment. Based on the relationship between the width of a molten pool and true weld width, colored measurement noise is recognized as a source of errors, and the Kalman filter algorithm is suitable for eliminating noise errors. In addition, complex fluxion of a molten pool leads to the nonlinear variation between the width of the molten pool and that of the welding bead, which is another source of errors during laser-MIG hybrid welding. Therefore, a BP neural network is chosen to predict the nonlinear difference between the width of Kalman optimal estimation and the true weld width, so that the errors caused by the fluctuation of the molten pool can be further restrained. Experimental results demonstrate that using a compensating colored measurement noise Kalman filter algorithm, which is compensated by the BP neural network, can reduce weld width detection errors better than other methods and can improve the detection accuracy. Compared with the Kalman filter algorithm, the BP neural network has a good nonlinear mapping ability, which can effectively improve the Kalman filter accuracy for weld width detection.

Key words laser technique; neural network; laser-MIG hybrid welding; weld width prediction; strong noise; Kalman filter